iScience

CellPress
OPEN ACCESS

Article

Biosugarcane-based carbon support for high-performance iron-based Fischer-Tropsch synthesis

Jingyang Bai, Chuan Qin, Yanfei Xu, Yixiong Du, Guangyuan Ma, Mingyue Ding

dingmy@whu.edu.cn

Highlights

A kind of carbon support, derived from the sugarcane bagasse, is prepared

This biochar catalyst reaches an excellent FTY value in Fischer-Tropsch synthesis

Functional groups and Fe species sizes regulate metal-support interactions

Superior performance is due to abundant functional groups and ε-Fe_2C

Bai et al., iScience 24, 102715
July 23, 2021
https://doi.org/10.1016/j.isci.2021.102715

iScience

CellPress
OPEN ACCESS

Article

Biosugarcane-based carbon support for high-performance iron-based Fischer-Tropsch synthesis

Jingyang Bai,[1,3] Chuan Qin,[1,3] Yanfei Xu,[1] Yixiong Du,[1] Guangyuan Ma,[1] and Mingyue Ding[1,2,4,*]

SUMMARY

Exploiting new carbon supports with adjustable metal-support interaction and low price is of prime importance to realize the maximum active iron efficiency and industrial-scale application of Fe-based catalysts for Fischer-Tropsch synthesis (FTS). Herein, a simple, tunable, and scalable biochar support derived from the sugarcane bagasse was successfully prepared and was first used for FTS. The metal-support interaction was precisely controlled by functional groups of biosugarcane-based carbon material and different iron species sizes. All catalysts synthesized displayed high activities, and the iron-time-yield of Fe_4/C_{bio} even reached 1,198.9 μmol g_{Fe}^{-1} s^{-1}. This performance was due to the unique structure and characteristics of the biosugarcane-based carbon support, which possessed abundant C−O, C=O (η^1(O) and η^2(C, O)) functional groups, thus endowing the moderate metal-support interaction, high dispersion of active iron species, more active ε-Fe_2C phase, and, most importantly, a high proportion of Fe_xC/Fe_{surf}, facilitating the maximum iron efficiency and intrinsic activity of the catalyst.

INTRODUCTION

Fischer-Tropsch synthesis (FTS) is an essential approach to produce liquid fuels and a variety of value-added chemicals from non-petroleum carbon resources (Khodakov et al., 2007; Ojeda et al., 2010; Weststrate et al., 2020; Zhang et al., 2020; Wu et al., 2017; Mosayebi and Haghtalab, 2015). With the rising energy demand and growing concerns about oil depletion, extensive efforts have been devoted to improving the catalytic performance and slashing the cost of FTS in recent years (Zhang et al., 2010; Phanopoulos et al., 2020; Kang et al., 2011; Lyu et al., 2020a; Liu et al., 2019). Among several common FTS catalysts (Fe-, Co-, and Ru-based catalysts), support Fe catalysts are preferentially used in commercial FTS plants because of their low cost, high activity, wide temperature, and H_2/CO ratio adaptability (230–350°C, H_2/CO = 0.5–2.5), which can be operated in a more flexible condition and even suitable for the conversion of the biomass-derived syngas (H_2/CO ≈ 1) (Liu et al., 2010; Wang and Astruc, 2017; Wang et al., 2018).

Generally, in order to achieve a high CO conversion rate, iron contents in industrial catalysts are usually maintained at 40–50 wt%(Liu et al., 1997). However, the high metal loading leads to larger particle sizes of iron species, resulting in a lower iron efficiency (reflected by iron-time-yield (FTY); moles of CO converted to hydrocarbons per gram of iron per second). But when the low metal loadings are used, owing to the strong metal-support interaction, part of the iron forms mixed oxides (such as iron silicates and titanates) that are hardly reducible and not active for FTS, thus suppressing the formation of iron carbides during reaction processes and still resulting in a low FTY. Therefore, precise control of metal-support interaction to achieve efficient carburization of iron species with small particle sizes remains a severe challenge that limits the high utilization of Fe-based FTS catalysts.

To tackle this issue, the prerequisite is to find an appropriate support that provides moderate metal-support interaction and tunable surface chemistry. Compared with various oxide support (including TiO_2, SiO_2, Al_2O_3, CeO_2, ZrO_2), carbon materials are excellent candidates owing to their unique properties of chemically inertness, high specific surface area, weaker metal-support interactions, adjustable texture, and surface chemistry (Gerber and Serp, 2020; Lam and Luong, 2014). In addition, directly introducing the iron on carbon supports offers an intimate contact between Fe and C, promoting the formation of iron carbides, which are well known to be the active phase in FTS (Li et al., 2001). To date, a variety of carbonaceous materials such as activated carbon (AC), carbon nanofibers, carbon nanotubes (CNTs), and carbon

[1]School of Power and Mechanical Engineering, the Institute of Technological Sciences, Wuhan University, Wuhan 430072, China

[2]Shenzhen Research Institute of Wuhan University, Shenzhen 518108, China

[3]These authors contributed equally

[4]Lead contact

*Correspondence: dingmy@whu.edu.cn

https://doi.org/10.1016/j.isci.2021.102715

microspheres have been employed as supports for iron catalysts (Zhang et al., 2018; Tan et al., 2018; Zhu et al., 2017). These catalysts demonstrated a high FTY and selectivity to C_{5+} hydrocarbons in FTS owing to the high dispersion and reducibility of iron species (Chen et al., 2015). However, problems like poor stability, high price, catalyst agglomeration, and sintering caused by the weak metal-support interaction still remain and limit the use of carbon supports on an industrial scale (Chernyak et al., 2020; Lin et al., 2017; Cheng et al., 2016). Hence, exploring new carbon materials with adjustable metal-support interaction and low price to achieve maximum iron utilization efficiency and attractive FTS performance is of prime importance.

Sugarcane bagasse, a typical agricultural waste, which contains hierarchical pore structure and extensive functional groups exposed, has been considered as a promising biomass-based carbon precursor (Zou et al., 2018; Feng et al., 2016; Hao et al., 2014). In addition, it has tempting merits like abundant availability, environmental friendliness, and low cost (Tao et al., 2015; Foo et al., 2013). Because of these characteristics, the biochar derived from sugarcane bagasse has been applied in adsorption (Lyu et al., 2018; Noreen et al., 2020; Lan et al., 2020; Ahmad et al., 2018), gas capture (Guo et al., 2020; Han et al., 2019; Srenscek-Nazzal et al., 2013), supercapacitor (Deng et al., 2016; Hao et al., 2014; Feng et al., 2016), and other catalytic reactions (Park et al., 2018; Li et al., 2017; Liu et al., 2018; Kuo et al., 2020). In this study, a series of biosugarcane-based Fe/C catalysts are synthesized by a simple impregnation method and first used in FTS. These catalysts showed remarkable FTS performance compared with the reference Fe_4/AC catalyst or other reported catalysts. At a low iron loading of 4 wt%, the FTY of Fe_4/C_{bio} was as high as 1,198.9 μmol g_{Fe}^{-1} s^{-1}. Combining the detailed characterizations of the blank supports and the fresh and spent catalysts, the structure-performance relationship of the biosugarcane-based Fe/C_{bio} catalysts was explored and revealed.

RESULTS AND DISCUSSION

Synthesis and structures of biosugarcane-based carbon support

The sugarcane bagasse used in this study contained 47.2% of carbon, 5.7% of hydrogen, 0.7% of nitrogen, and a certain amount of trace elements (confirmed by the EA and ICP-OES, Table S1). First, to determine an appropriate pyrolysis temperature, the thermogravimetry and differential thermogravimetry analysis was carried out on this biomass-based carbon precursor. It could be seen that, with increasing temperature, there were two main steps of mass loss occurring at 250°C–300°C and 300°C–400°C (Figure 1A), which were ascribed to the continuous decomposition of oxygen-containing functional groups from biosugarcane (Yan et al., 2013). After that, a slow carbonization process still happened until 800°C since all the groups of biosugarcane were eliminated at this temperature. In order to retain a proper amount of functional groups, while removing some active oxygen-containing compounds, pyrolysis of bagasse was carried out at 450°C.

The elements content of C_{bio} after pyrolysis was shown in Table S2. The X-ray diffraction (XRD) pattern of the sample (Figure 1B) displayed a typical broad peak around $2\theta = 23.0°$, corresponding to the (002) reflection of the disordered carbon (Liu et al., 2016), which demonstrated that the biosugarcane-based carbon support was successfully synthesized. Meanwhile, the Raman spectrum in Figure 1C possessed two carbon characteristic peaks at 1,350 and 1,590 cm^{-1}, also illustrating the formation of carbon materials (Chmiola et al., 2006). Scanning electron microscopy (SEM) analysis showed that the morphology of the biosugarcane-based carbon support (Figures 1D and 1E) was a kind of 3D hierarchical pore structure with multi-channels, which was preserved from the sugarcane bagasse during the pyrolysis process (Figure S1). Figure 1D shows a honeycomb porous structure for the C_{bio} in cross section, which existed in the large-lumen vessels, fiber tracheids, and thin cell walls. As shown in Figure 1E, there are also a lot of tiny holes and pits on the side of the C_{bio} (Tao et al., 2020). The support with 3D hierarchical pore structure can facilitate the dispersion of the iron particles and the transfer of the raw materials and products from both horizontal and vertical directions. The textural properties of this support were depicted in Figure S2 and Table 1. The specific surface area and average pore volume were 112.0 m^2 g−1 and 0.43 cm^3 g−1, respectively. The pore size distribution shows that the C_{bio} has abundant meso- and micro-pores owing to its 3D hierarchical pore structure with multi-channels.

The functional groups of the biosugarcane-based carbon support were detected by Fourier transform infrared (FTIR, Figure 1F). The characteristic peaks from 803 to 2,923 cm^{-1} were assigned to the carbon-containing functional groups, including aromatic C−H, C−O, C=O, C−H, and $-CH_2-$, and the peak at 3,430 cm^{-1} was attributed to the hydroxyl stretching vibration (Luo et al., 2018). These functional groups

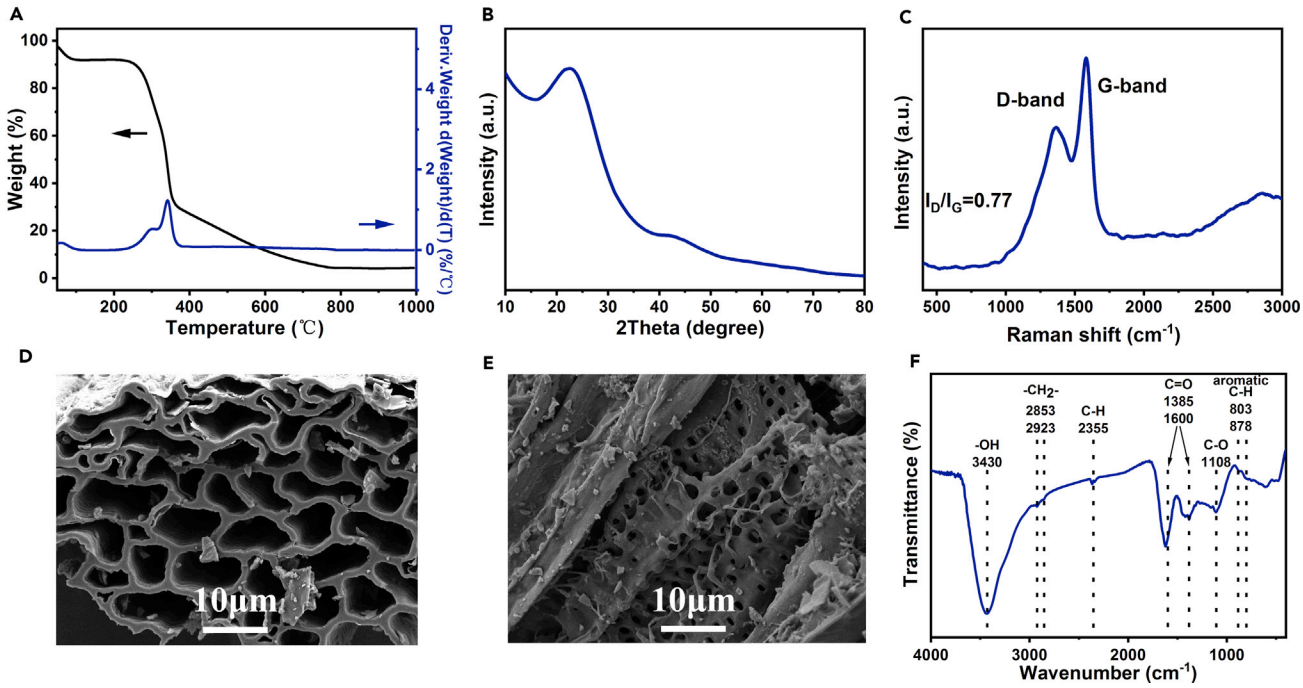

Figure 1. Characterization of biosugarcane-based carbon support

(A) TG (black) and DTG (blue) curves, (B) XRD pattern, (C) Raman pattern, SEM images (D) in cross section and (E) on the side, and (F) FTIR spectrum of the blank sample after pyrolysis.

were beneficial for uniform adsorption and dispersion of metal ions and contributed to suppressing the agglomeration of nanoparticles during the pyrolysis process (Tao et al., 2020). Such a biosugarcane-based carbon support with 3D hierarchical pore structure and appropriate amount of functional groups was expected to endow Fe-based catalysts with excellent FTS performance.

Characterization of biosugarcane-based Fe/C_{bio} catalysts

As the 1, 4, 8, and 12 wt% of Fe loaded, in addition to the above mentioned XRD diffractions of the carbon material, additional peaks at 30.2, 35.5, 43.2, 57.1, and 62.7° corresponding to the characteristic of Fe_3O_4 (PDF No. 88-0315) emerged when the Fe loading exceeds 4 wt% (Figure 2A). This phenomenon indicated that Fe_3O_4 species were highly dispersed at low loadings, whereas they formed crystallites at high loadings. The Fe_3O_4 crystallite size in the high Fe content catalysts was estimated using the Debye-Scherrer equation based on the analysis of the Fe_3O_4 (311) plane at 35.5°, and the crystallite sizes of Fe_3O_4 species in the Fe_8/C_{bio} and Fe_{12}/C_{bio} were 4.5 and 6.2 nm, respectively, suggesting that larger Fe_3O_4 crystallites existed in the higher Fe content samples.

The Raman spectra of catalysts were shown in Figure 2B; two bands at 1,350 and 1,590 cm^{-1} reflected the disordered (D-band) and graphitic (G-band) structures of carbon, respectively (Chmiola et al., 2006). It was well accepted that the intensity ratio of I_D/I_G was a good indicator of the disorder degree of carbon

Table 1. Specific surface area, pore size, and pore volume of the blank sample and as-prepared catalysts

Catalyst	Surface area (m^2 g^{-1})	Pore size (nm)	Pore volume (cm^3 g^{-1})
C_{bio}	112.0	4.6	0.43
Fe_1/C_{bio}	53.7	4.5	0.15
Fe_4/C_{bio}	34.3	4.3	0.11
Fe_8/C_{bio}	27.2	4.7	0.10
Fe_{12}/C_{bio}	24.0	5.0	0.14

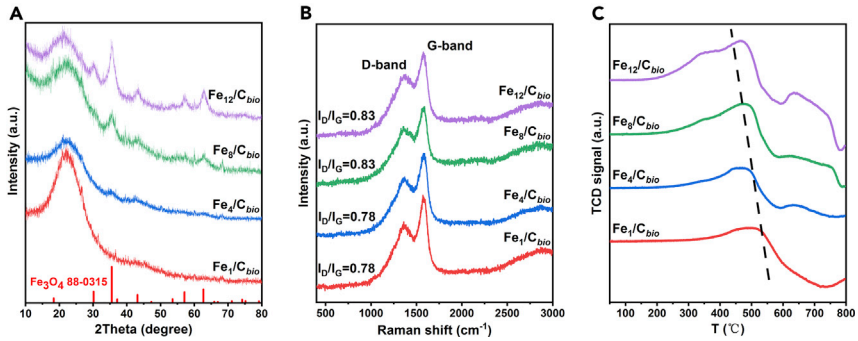

Figure 2. Characterization of Fe/C_{bio} catalysts.

(A) XRD patterns, (B) Raman pattern, and (C) H_2-TPR spectra of the as-prepared catalysts.

materials (Hu et al., 2017). In this study, the I_D/I_G values of catalysts upshifted from 0.78 to 0.83 as the iron content increased, indicating that introduced iron ions might be distributed in the carbon matrix by linking to surface functional groups, thus inhibiting the generation of graphitized carbon from amorphous carbon and causing a more disordered structure (Zhang et al., 2014).

To reveal the exact distributing location of iron species in the biosugarcane-based carbon support, FTIR spectra of the blank support and representative Fe_4/C_{bio} catalyst were analyzed and compared. The specific spectrum was shown in the later part (see Figure 6). It was seen that, after the iron loading, the bands of surface functional groups including C=O (1,385 cm^{-1}) and C−O (1,108 cm^{-1}) decreased sharply, demonstrating that iron species were distributed in the biosugarcane carbon matrix by combining with the surface C=O and C−O functional groups.

SEM analysis (Figures 3A–3H) showed that all catalysts displayed analogous 3D hierarchical morphologies with no obvious changes from the pure support. The energy-dispersive X-ray spectroscopy mapping images of the low-Fe-content catalysts (Fe_4/C_{bio}, Figures 3I–3L) revealed that Fe species were highly dispersed on the biosugarcane-based carbon support, which was consist with the above XRD results that the diffractions of Fe_3O_4 were only observed at high Fe loadings. High-resolution transmission electron microscopy (HRTEM) analysis (Figure 4) indicated that particle sizes of Fe species were quite uniform with a narrow size distribution, and the average size of Fe species showed an increase from 1.5 to 4.6 nm as the Fe loading increased from 1 to 12 wt%. In addition, with the adding of Fe content, the specific surface area of samples presented a decreasing trend (Table 1), which was attributed to part of micropores being filled or blocked by Fe species (Wang et al., 2019b).

The metal-support interaction of the investigated catalysts was studied by temperature-programmed reduction in H_2 (H_2-TPR). As shown in Figure 2C, all profiles exhibited a broad hydrogen consumption peak at 300–550°C and a negative peak over 600°C. The first peak was due to the reduction of Fe_3O_4 (Suo et al., 2012), whereas the high-temperature characteristic peak was attributed to the hydrogenation and decomposition of the biomass-based carbon support, releasing H_2 and causing the negative TPR signal. It was observed that the maximum temperature of the reduction peak shifted gradually toward lower temperature with the adding of Fe species, suggesting the weakened interaction of Fe_3O_4−C_{bio} support and the improved reducibility of catalysts. This could be explained by the fact that, with the increase of iron content, the particle size of iron species on catalysts increased correspondingly. At the same time, the dispersion of iron species decreased and larger particles had less interaction with the support, which tended to be reduced (Mogorosi et al., 2012).

Catalytic performance

The FTS performance of the catalysts was evaluated under an identical weight hourly space velocity (WHSV = 20,000 mL h^{-1} g^{-1}) and reaction temperature (300°C). First, the blank test of C_{bio} was conducted to prove that the carbon support had no FTS activity. The detailed evaluation results of the Fe_χ/C_{bio} catalysts were depicted in Table 2 and Figure 5B. It could be seen that the CO conversion of catalysts following the order Fe_1/C_{bio} (4.9%) < Fe_4/C_{bio} (80.9%) < Fe_8/C_{bio} (85.7%) < Fe_{12}/C_{bio} (90.9%), which was reasonable

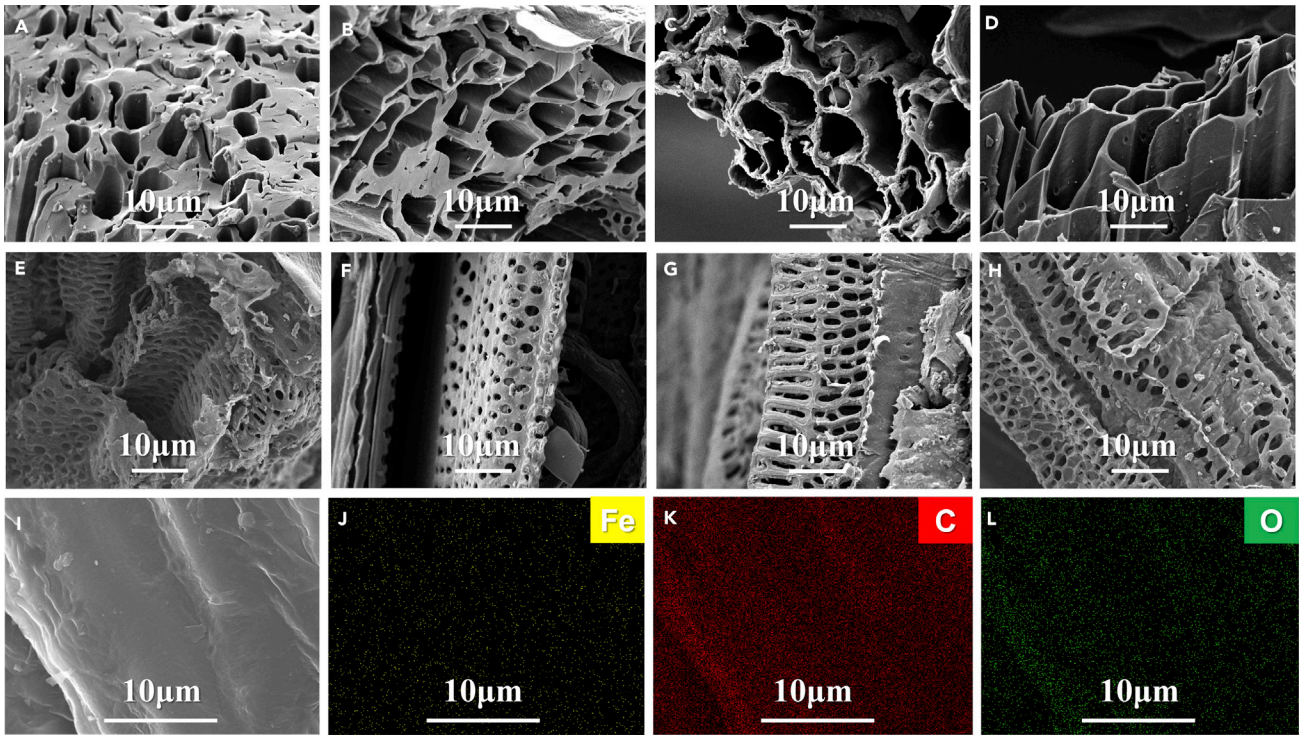

Figure 3. SEM images and EDS images of Fe/C_{bio} catalysts

SEM images of the (A, E) Fe_1/C_{bio}, (B, F) Fe_4/C_{bio}, (C, G) Fe_8/C_{bio}, (D, H) Fe_{12}/C_{bio} catalysts, and energy-dispersive X-ray spectroscopy element mappings images of (I) SEM image, (J) Fe, (K) C, and (L) O of the Fe_4/C_{bio} catalysts.

for the increasing of the iron loading. The 4-fold increase of the Fe loading from Fe_1/C_{bio} to Fe_4/C_{bio} and the upper limit of the reaction conversion might result in such a soaring from Fe_1/C_{bio} to Fe_4/C_{bio}. However, the FTY of catalysts, which represented the intrinsic catalytic activities, was not equal to each other. When FTY was plotted as a function of the iron content, a volcano-like curve was obtained with an optimum iron loading of 4 wt% (Figure 5A). In addition, compared with the various literature catalysts (Table 3), all bio-sugarcane-based Fe/C_{bio} catalysts synthesized in this study displayed significantly higher FTY values, and the FTY of Fe_4/C_{bio} even reached 1,198.9 μmol g_{Fe}^{-1} s^{-1}. These results indicated that the bio-sugarcane-based carbon support had great advantages over other reported supports. The reasons for the outstanding performance of biosugarcane-based Fe/C_{bio} catalysts are discussed later.

In addition, all catalysts presented a similar product distribution following the Anderson-Schulz-Flory statistics. And the calculated chain growth probability α (Figure S3) agreed well with the previous studies. Furthermore, the stability of the Fe_4/C_{bio} catalyst was investigated over a time on stream of 150 h. It can be seen from Figure 5C that Fe_4/C_{bio} exhibited an excellent stability and a sustained product selectivity throughout the reaction process. This striking performance and the simplicity of the preparation method demonstrated great potential for the application of biosugarcane-based carbon materials for FTS in a large scale.

Key reasons for the performance of biosugarcane-based Fe/C_{bio} catalysts

The aforementioned results demonstrated that all biosugarcane-based Fe/C_{bio} catalysts synthesized in this study displayed significantly high activities among literature catalysts. Considering that only the simple impregnation method was used, these results indicated that the biosugarcane-based carbon support with 3D hierarchical pore structure, which possessed abundant C=O, C−O functional groups and endowed moderate metal-support interaction and high dispersion of active species, seemed to be the key reason for the improved catalytic performance. To verify this speculation, we prepared a reference catalyst (denoted as Fe_4/AC) by replacing the biosugarcane support with AC. The FTS performance of Fe_4/AC was evaluated under the same procedure performed on Fe_4/C_{bio}. It was observed that at an identical reaction

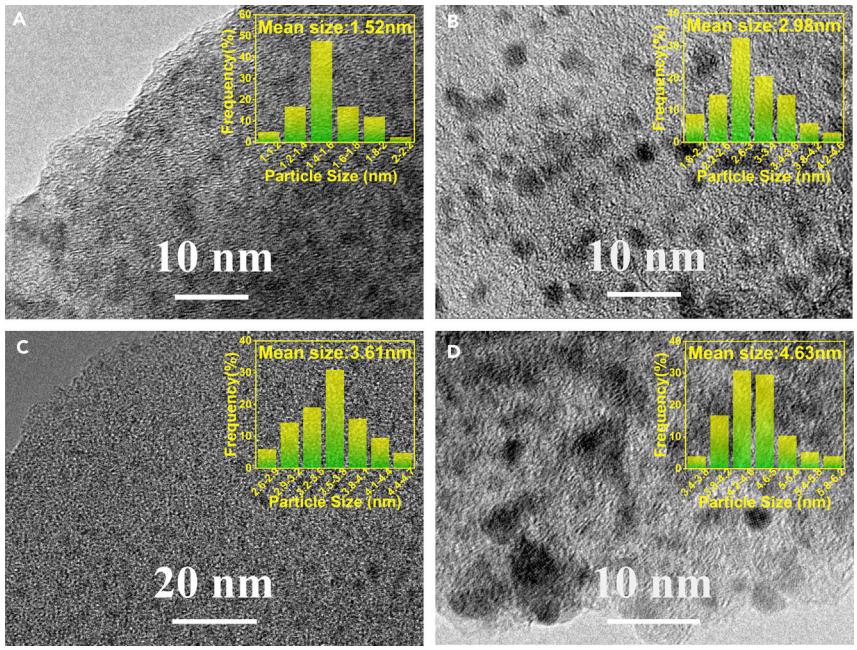

Figure 4. HRTEM images of Fe/C_{bio} catalysts

HRTEM images of the (A) Fe_1/C_{bio}, (B) Fe_4/C_{bio} catalysts, (C) Fe_8/C_{bio}, and (D) Fe_{12}/C_{bio} catalysts.

temperature (300°C) and WHSV (20,000 mL h^{-1} g^{-1}), the CO conversion of Fe_4/AC was low to 12.6% (Table 2), and the FTY was 286.6 μmol g_{Fe}^{-1} s^{-1}. This was a commonly reported level of AC carrier in the literature and was far less than the catalysts derived from the biosugarcane-based carbon support in this work. These results indicated that the biosugarcane-based carbon material was indeed an excellent support for high FTS performance.

In order to further explore the uniqueness of this biomass support, the FTIR spectra of C_{bio} and AC were compared (Figure 6). Both supports showed the bands at 1,108 and 1,600 cm^{-1}, which corresponded to the surface C–O and C=O (η^1(C, O) configuration). Nevertheless, AC barely showed the band (1,385 cm^{-1}) corresponding to surface C=O (η^2(C, O) configuration). The η^2(C, O) configuration (both C and O atoms interacting with an intrinsic surface metal) was considered a stronger carbonyl surface bond than the η^1(C, O) configuration (O atoms of carbonyl linearly coordinates with surface metal atoms) (Sitthisa et al., 2011). These results indicated that C_{bio} had more modes of functional groups to interact with metal nanoparticles than AC.

Moreover, after the iron loading, the bands of C=O (η^1(C, O) and η^2(C, O) configuration) and C–O functional groups over C_{bio} decreased sharply, indicating that iron species were distributed in C_{bio} by

Table 2. FTS results of the as-prepared catalysts

		CO_2 and hydrocarbons product selectivity (mol %)				FTY
Catalyst	CO conv. (%)	CO_2	CH_4	C_2–C_4	C_{5+}	μmol g_{Fe}^{-1} s^{-1}
C_{bio}	0	–	–	–	–	–
Fe_1/C_{bio}	4.9	18.3	24.2	42.5	15.0	506.5
Fe_4/C_{bio}	80.9	48.6	11.6	22.3	17.5	1,198.9
Fe_8/C_{bio}	85.7	49.8	14.7	23.9	11.6	611.7
Fe_{12}/C_{bio}	90.9	49.2	15.0	25.4	10.4	411.3
Fe_4/AC	12.6	21.6	19.6	36.0	22.8	286.6

Catalyst tests performed at 300°C, 2.0 MPa, WHSV = 20,000 mL h^{-1} g^{-1}, H_2/CO ratio = 1.

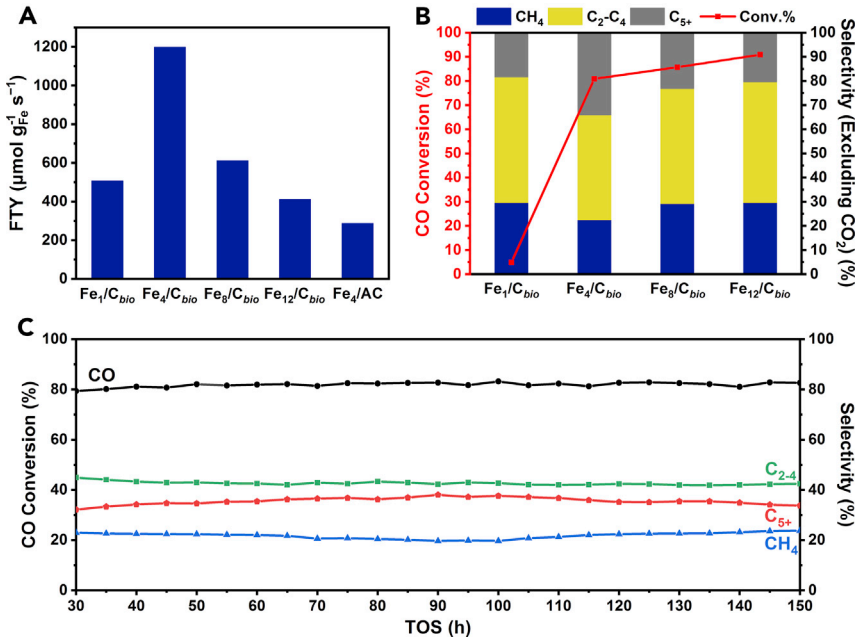

Figure 5. FTS performance of Fe/C_{bio} catalysts

(A) FTY, (B) CO conv. % and products selectivity of FTS results of the as-prepared catalysts, and (C) the stability of the Fe_4/C_{bio} catalyst over a time on stream of 150 h.

combining with the surface C=O and C−O functional groups. While for AC, apart from the lacking C=O (η^2(C, O) configuration) peaks, the intensity of the other two peaks over AC almost did not have any change. These results revealed that the nanoparticles interacted with C_{bio} via more functional groups than AC. In addition, the XRD results (Figure S4) showed that the intensity of Fe_3O_4 characteristic peak over Fe_4/C_{bio} was weaker than that over Fe_4/AC, indicating that, at the same Fe loadings, Fe_4/C_{bio} possessed smaller particle sizes of Fe_3O_4 species and higher dispersion than Fe_4/AC.

The XRD results of the spent Fe_χ/C_{bio} catalysts (Figure 7A) showed that, after the FTS process, the characteristic peaks of Fe_3O_4 were evidently decreased and the additional peaks at 37.7°, 41.5°, 43.2°, 57.3°, and 68.0° corresponding to the characteristic of ε-Fe_2C (PDF No. 36-1249) emerged. The HRTEM image and the corresponding FFT pattern of spent Fe_4/C_{bio} (Figure S5) also proved that the measured lattice spacings of 0.21 nm corresponded to the (101) planes of ε-Fe_2C. Recent works (Lyu et al., 2020b; Xu et al., 2014) had shown that ε-Fe_2C was a more active phase than χ-Fe_5C_2 in FTS and this was another significant reason for the high performance of biosugarcane-based Fe_χ/C_{bio} catalysts. And the formation of ε-Fe_2C was not a coincidence. Previous works had revealed the relationship between metal particle size and the formed iron carbide phase as well as that ε-Fe_2C was prone to form with smaller iron particles (Raupp and Delgass, 1979). As C_{bio} derived from sugarcane bagasse can offer more active sites, refine the agglomeration of metal nanoparticles, and improve further the dispersion of metal nanoparticles, the metal particle size was very small during FTS, which was conducive to the formation of ε-Fe_2C. Therefore, a high FTS activity over the biosugarcane-based Fe_χ/C_{bio} catalysts might be attributed to the following reasons: (1) The C_{bio} support with 3D hierarchical pore structure provided more kinds and modes of functional groups to interact with metal nanoparticles than the conventional AC, which helped to offer more active sites, refine the agglomeration of metal nanoparticles, and improve the dispersion of metal nanoparticles. (2) The formation of ε-Fe_2C, which was the main iron carbide phase existing in the Fe_χ/C_{bio} catalysts, provided more active sites for FTS.

Key factors for the performance enhancement of the low loading Fe_4/C_{bio} catalyst

Except the advantages of the above Fe_χ/C_{bio} catalyst, in order to reveal why the low loading Fe_4/C_{bio} catalyst possessed the highest catalytic activity, the spent catalysts were further studied and discussed. The XRD results of the spent catalysts (Figure 7A) showed that the peak intensity of ε-Fe_2C increased gradually

Table 3. Comparison of the FTY results in FTS

Catalyst	Reaction condition				CO conv. %	FTY μmol g_{Fe}^{-1} s^{-1}	Reference
	T °C	P MPa	H_2/CO	WHSV ml h^{-1} g^{-1}			
Fe_1/C_{bio}	300	2.0	1	20,000	4.9	506.5	This work
Fe_4/C_{bio}	300	2.0	1	20,000	80.9	**1,198.9**	
Fe_8/C_{bio}	300	2.0	1	20,000	85.7	611.7	
Fe_{12}/C_{bio}	300	2.0	1	20,000	90.9	411.3	
Fe_4/AC	300	2.0	1	20,000	12.6	286.6	
FeKCa1.0/Al_2O_3	340	1.0	1	9,000	75.1	288	(Wang et al., 2019a)
Fe@C-400	340	2.0	1	30,000	74.0	380	(Wezendonk et al., 2016)
Fe_5C_2@C	320	1.5	1	8,000	96.0	150	(Hong et al., 2015)
25-Fe@C (Fe = 25 wt%)	340	2.0	1	30,000	59.0	490	(Santos et al., 2015)
Fe/NCNT (Fe = 16.1 wt%)	340	2.5	1	50,000	56.5	780	(Chew et al., 2016)
Fe-MIL-88B-NH2/C (Fe = 32–34 wt%)	300	2.0	1	180,000	27.8	720	(An et al., 2016)
	300	2.0	1	36,000	81.8	320	(An et al., 2016)
Fe/G-C	340	2.0	2	8,000	90.2	292.7	(Wei et al., 2020)
10FeSi50	300	2.0	2	16,200	33.8	203.6	(Cheng et al., 2015)

with the increase of iron loading, suggesting that larger ε-Fe_2C crystallites existed in the higher-iron-content catalysts. The H_2-TPD results also indicated that the Fe_4/C_{bio} had a highest Fe dispersion of 18.32% (Table S4). For Fe dispersion of Fe_1/C_{bio} catalyst, the decline of calculation result may be due to the difficulty of reduction and the partial coverage or embedding of the support by the strong metal-support interaction (Tauster et al., 1981; van Deelen et al., 2019; Willinger et al., 2014). And a proper iron loading (Fe_4/C_{bio}) would lead to an appropriate particle size and a moderate metal-support interaction that is beneficial to improve the intrinsic activity of the catalyst.

The chemical composition and elemental state of the spent catalysts were examined by X-ray photoelectron spectroscopy (XPS). The full XPS spectra (Figure S6) revealed that all spent Fe/C_{bio} catalysts consisted of the elements Fe, O, and C. In the Fe 2*p* spectrum (Figure 7C), two obvious peaks observed at 711.7 and 723.8 eV belonged to the binding energy of Fe $2p_{3/2}$ and Fe $2p_{1/2}$, respectively (Yang et al., 2012). Curve fitting of this Fe 2*p* spectrum indicated that both Fe^{2+} and Fe^{3+} species existed on the surface of catalysts, which manifested the existence of Fe_3O_4 (Tan, 2016). Another peak that assigned to iron carbides arose at 708 eV (Zhao et al., 2018). The ratio of iron carbide to surface iron (Fe_xC/Fe_{surf}) was determined by calculating the relative amount of iron carbides and iron. The sequence of Fe_xC/Fe_{surf} was Fe_4/C_{bio} (18.5%) > Fe_8/C_{bio} (12.1%) > Fe_1/C_{bio} (11.2%) > Fe_{12}/C_{bio} (9.8%), which correlated well with the activity trend observed in the FTS. To provide further evidence for this relationship, the variation of FTY was plotted as a function of the value of Fe_xC/Fe_{surf} (Figure 7B). It was found that there was a significant positive

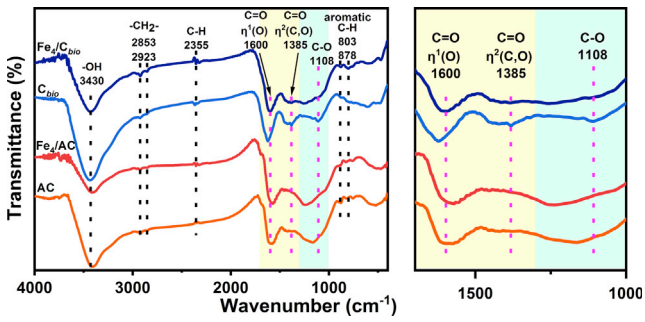

Figure 6. FTIR spectrum of the Fe_4/C_{bio}, C_{bio}, Fe_4/AC, and AC.

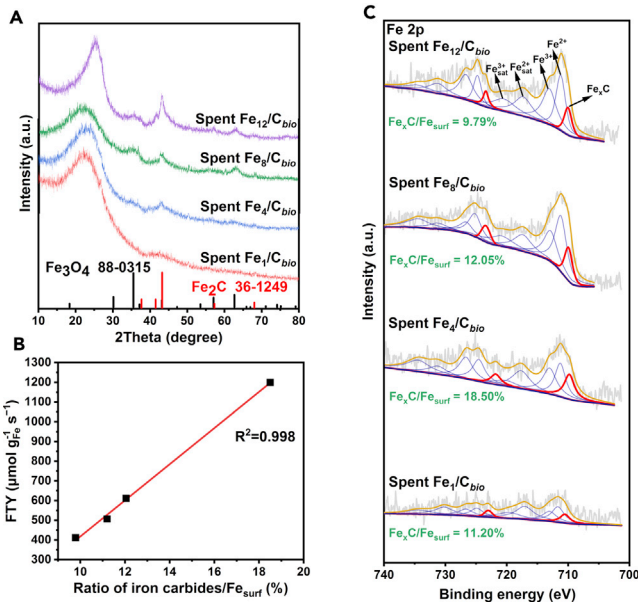

Figure 7. Characterization of the spent Fe/C_{bio} catalysts

(A) XRD patterns, (B) the relationship between FTY and iron carbides ratio, and (C) XPS patterns of Fe 2*p* of the spent catalysts after FTS.

correlation between the FTY and the ratio of Fe_xC/Fe_{surf}, which meant that the proportion of iron carbides was directly correlated with the reaction activity. And when the iron loading was 4 wt%, the proportion of iron carbides in the catalyst that really worked was the highest, which explained why the Fe_4/C_{bio} catalyst had the highest intrinsic activity.

Overall, the phenomenon that the FTY of catalysts presented a parabolic tendency with the increase of iron loading was related to the efficiency of converting iron to active sites. As for the low loading of Fe species (Fe_1/C_{bio}), it had the characteristics of strong metal-support interaction and was relatively difficult to reduce, so active species would be less correspondingly, leading to a low FTS reactivity. With the increase of the iron loading, the catalytic activity increased and reached a peak (4 wt% in this study). When the iron loading increased continually, so did the particle size of iron species. Iron carbides with large particle sizes had a smaller Fe dispersion and percentage of surface atoms than that of small iron carbides. And then, fewer surface atoms had the probability to contact with reactants during FTS, leading to a gradual decline in catalytic activity. Therefore, the optimum iron loading for the biosugarcane-based carbon support was 4 wt%.

Conclusion

In conclusion, a kind of biochar support with 3D hierarchical pore structure, which derived from the sugarcane bagasse, was successfully prepared and first used for FTS. Although only the simple impregnation method was used, all synthesized biosugarcane-based Fe/C_{bio} catalysts showed excellent FTS performance. Especially, the Fe_4/C_{bio} catalyst reached a high catalytic activity (1,198.9 μmol g_{Fe}^{-1} s^{-1}) and excellent stability (TOS = 150 h). The key factors for the superiority of biosugarcane-based Fe/C_{bio} catalysts were

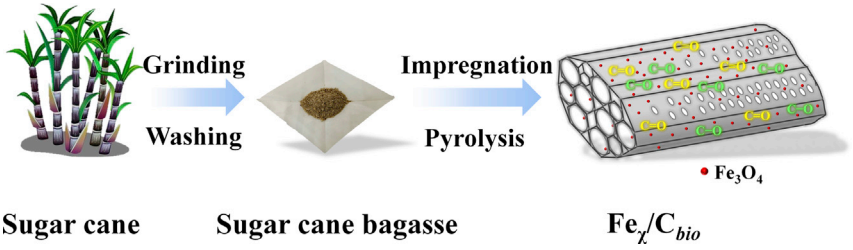

Scheme 1. The synthesis procedure of Fe_x/C_{bio} catalysts

also investigated and elucidated. These findings demonstrated that the catalytic performance of FTS could be significantly enhanced by precise control of surface functional groups and the metal-support interaction and opened up a new avenue to rationally design the high-performance FTS catalysts. Meanwhile, other biomass wastes with similar properties also have promising prospect to be applied to FTS on a large scale.

STAR★METHODS

Detailed methods are provided in the online version of this paper and include the following:

- KEY RESOURCES TABLE
- RESOURCE AVAILABILITY
  - Lead contact
  - Materials availability
  - Data and code availability
- METHOD DETAILS
  - 1. Catalyst preparation
  - 2. Catalyst characterization
  - 3. Catalyst evaluation

SUPPLEMENTAL INFORMATION

Supplemental information can be found online at https://doi.org/10.1016/j.isci.2021.102715.

ACKNOWLEDGMENTS

The authors gratefully acknowledge the financial support from the National Natural Science Foundation of China (21978225, 51861145102), National Key Research and Development Plan of China (2018YFE0125200), Guangdong Provincial Science and Technology Project (2019A050510031), Science and Technology program of Shenzhen (JCYJ20180302153928437, JCYJ20190808150418994).

AUTHOR CONTRIBUTIONS

Conceptualization, J.B. and C.Q.; methodology, M.D., C.Q., J.B.; investigation, J.B., C.Q., Y.X., and Y.D.; formal analysis, J.B., C.Q., and Y.X.; writing – original draft, J.B. and C.Q.; writing – review & editing, C.Q. and J.B.; resources, G.M. and F.X.; supervision, M.D.

DECLARATION OF INTERESTS

The authors declare no competing interests.

Received: March 22, 2021
Revised: May 6, 2021
Accepted: June 7, 2021
Published: July 23, 2021

REFERENCES

Ahmad, Z., Gao, B., Mosa, A., Yu, H., Yin, X., Bashir, A., Ghoveisi, H., and Wang, S. (2018). Removal of Cu(II), Cd(II) and Pb(II) ions from aqueous solutions by biochars derived from potassium-rich biomass. J. Clean. Prod. *180*, 437–449.

An, B., Cheng, K., Wang, C., Wang, Y., and Lin, W. (2016). Pyrolysis of metal-organic frameworks to Fe3O4@Fe5C2 core-shell nanoparticles for Fischer-Tropsch synthesis. Acs Catal. *6*, 3610–3618.

Chen, X.Q., Deng, D.H., Pan, X.L., and Bao, X.H. (2015). Iron catalyst encapsulated in carbon nanotubes for CO hydrogenation to light olefins. Chin. J. Catal. *36*, 1631–1637.

Cheng, K., Virginie, M., Ordomsky, V.V., Cordier, C., Chernavskii, P.A., Ivantsov, M.I., Paul, S., Wang, Y., and Khodakov, A.Y. (2015). Pore size effects in high-temperature Fischer-Tropsch synthesis over supported iron catalysts. J. Catal. *328*, 139–150.

Cheng, Y., Lin, J., Xu, K., Wang, H., Yao, X.Y., Pei, Y., Yan, S.R., Qiao, M.H., and Zong, B.N. (2016). Fischer-Tropsch synthesis to lower olefins over potassium-promoted reduced graphene oxide supported iron catalysts. Acs Catal. *6*, 389–399.

Chernyak, S., Burtsev, A., Maksimov, S., Kupreenko, S., Maslakov, K., and Savilov, S. (2020). Structural evolution, stability, deactivation and regeneration of Fischer-Tropsch cobalt-based catalysts supported on carbon nanotubes. Appl. Catal. A *603*, 117741. https://doi.org/10.1016/j.apcata.2020.117741.

Chew, L.M., Xia, W., Duedder, H., Weide, P., Ruland, H., and Muhler, M. (2016). On the role of the stability of functional groups in multi-walled carbon nanotubes applied as support in iron-based high-temperature Fischer-Tropsch synthesis. Catal. Today *270*, 85–92.

Chmiola, J., Yushin, G., Gogotsi, Y., Portet, C., Simon, P., and Taberna, P.L. (2006). Anomalous increase in carbon capacitance at pore sizes less than 1 nanometer. Science *313*, 1760–1763.

Deng, Y., Xie, Y., Zou, K., and Ji, X. (2016). Review on recent advances in nitrogen-doped carbons: preparations and applications in supercapacitors. J. Mater. Chem. A *4*, 1144–1173.

Feng, H.B., Hu, H., Dong, H.W., Xiao, Y., Cai, Y.J., Lei, B.F., Liu, Y.L., and Zheng, M.T. (2016). Hierarchical structured carbon derived from bagasse wastes: a simple and efficient synthesis route and its improved electrochemical properties for high-performance supercapacitors. J. Power Sources *302*, 164–173.

Foo, K.Y., Lee, L.K., and Hameed, B.H. (2013). Preparation of activated carbon from sugarcane bagasse by microwave assisted activation for the remediation of semi-aerobic landfill leachate. Bioresour. Technol. *134*, 166–172.

Gerber, I.C., and Serp, P. (2020). A theory/experience description of support effects in carbon-supported catalysts. Chem. Rev. *120*, 1250–1349.

Guo, Y., Tan, C., Sun, J., Li, W., Zhang, J., and Zhao, C. (2020). Porous activated carbons derived from waste sugarcane bagasse for CO2 adsorption. Chem. Eng. J. *381*, 122736. https://doi.org/10.1016/j.cej.2019.122736.

Han, J., Zhang, L., Zhao, B., Qin, L., Wang, Y., and Xing, F. (2019). The N-doped activated carbon derived from sugarcane bagasse for CO2 adsorption. Ind. Crops Prod. *128*, 290–297.

Hao, P., Zhao, Z.H., Tian, J., Li, H.D., Sang, Y.H., Yu, G.W., Cai, H.Q., Liu, H., Wong, C.P., and Umar, A. (2014). Hierarchical porous carbon aerogel derived from bagasse for high performance supercapacitor electrode. Nanoscale *6*, 12120–12129.

Hong, S.Y., Chun, D.H., Yang, J.-I., Jung, H., Lee, H.-T., Hong, S., Jang, S., Lim, J.T., Kim, C.S., and Park, J.C. (2015). A new synthesis of carbon encapsulated Fe5C2 nanoparticles for high-temperature Fischer-Tropsch synthesis. Nanoscale *7*, 16616–16620.

Hu, L., Lu, Y., Li, X., Liang, J., Huang, T., Zhu, Y., and Qian, Y. (2017). Optimization of microporous carbon structures for Lithium-sulfur battery applications in carbonate-based electrolyte. Small *13*, 1603533. https://doi.org/10.1002/smll.201603533.

Kang, J.C., Cheng, K., Zhang, L., Zhang, Q.H., Ding, J.S., Hua, W.Q., Lou, Y.C., Zhai, Q.G., and Wang, Y. (2011). Mesoporous zeolite-supported ruthenium nanoparticles as highly selective fischer-tropsch catalysts for the production of C-5-C-11 Isoparaffins. Angew. Chem. Int. Ed. *50*, 5200–5203.

Khodakov, A.Y., Chu, W., and Fongarland, P. (2007). Advances in the development of novel cobalt Fischer-Tropsch catalysts for synthesis of long-chain hydrocarbons and clean fuels. Chem. Rev. *107*, 1692–1744.

Kuo, H.C., Liu, S.H., Lin, Y.G., Chiang, C.L., and Tsang, D.C.W. (2020). Synthesis of FeCo-N@N-doped carbon oxygen reduction catalysts via microwave-assisted ammoxidation. Catal. Sci. Technol. *10*, 3949–3958.

Lam, E., and Luong, J.H.T. (2014). Carbon materials as catalyst supports and catalysts in the transformation of biomass to fuels and chemicals. Acs Catal. *4*, 3393–3410.

Lan, T.Q., Zheng, W.Q., Dong, Y.F., Jiang, Y.X., Qin, Y.Y., Yue, G.J., and Zhou, H.F. (2020). Exploring surface properties of substrate to understand the difference in enzymatic hydrolysis of sugarcane bagasse treated with dilute acid and sulfite. Ind. Crops Prod. *145*, 112128. https://doi.org/10.1016/j.indcrop.2020.112128.

Li, P.J., Lin, K.R., Fang, Z.Q., and Wang, K.M. (2017). Enhanced nitrate removal by novel bimetallic Fe/Ni nanoparticles supported on biochar. J. Clean. Prod. *151*, 21–33.

Li, S.Z., Meitzner, G.D., and Iglesia, E. (2001). Structure and site evolution of iron oxide catalyst precursors during the Fischer-Tropsch synthesis. J. Phys. Chem. B *105*, 5743–5750.

Lin, B.Y., Guo, Y.J., Lin, J.D., Ni, J., Lin, J.X., Jiang, L.L., and Wang, Y. (2017). Deactivation study of carbon-supported ruthenium catalyst with potassium promoter. Appl. Catal. A *541*, 1–7.

Liu, B., Li, W.P., Xu, Y.B., Lin, Q., Jiang, F., and Liu, X.H. (2019). Insight into the intrinsic active site for selective production of light olefins in cobalt-catalyzed Fischer-Tropsch synthesis. Acs Catal. *9*, 7073–7089.

Liu, G.-H., Zong, Z.-M., Liu, Z.-Q., Liu, F.-J., Zhang, Y.-Y., and Wei, X.-Y. (2018). Solvent-controlled selective hydrodeoxygenation of bio-derived guaiacol to arenes or phenols over a biochar supported Co-doped MoO2 catalyst. Fuel Process. Technol. *179*, 114–123.

Liu, J., Deng, Y., Li, X., and Wang, L. (2016). Promising nitrogen-rich porous carbons derived from one-Step Calcium chloride activation of biomass-based waste for high performance supercapacitors. ACS Sustain. Chem. Eng. *4*, 177–187.

Liu, K., Suo, H., Zhang, C., Xu, J., Yang, Y., Xiang, H., and Li, Y. (2010). An active Fischer-Tropsch synthesis FeMo/SiO2 catalyst prepared by a modified sol-gel technique. Catal. Commun. *12*, 137–141.

Liu, Z.T., Li, Y.W., Zhou, J.L., Zhang, Z.X., and Zhang, B.J. (1997). Deactivation model of Fischer-Tropsch synthesis over an Fe-Cu-K commercial catalyst. Appl. Catal. A *161*, 137–151.

Luo, J., Li, X., Ge, C., Muller, K., Yu, H., Huang, P., Li, J., Tsang, D.C.W., Bolan, N.S., Rinklebe, J., and Wang, H. (2018). Sorption of norfloxacin, sulfamerazine and oxytetracycline by KOH-modified biochar under single and ternary systems. Bioresour. Technol. *263*, 385–392.

Lyu, H., Gao, B., He, F., Zimmerman, A.R., Ding, C., Tang, J., and Crittenden, J.C. (2018). Experimental and modeling investigations of ball-milled biochar for the removal of aqueous methylene blue. Chem. Eng. J. *335*, 110–119.

Lyu, S., Cheng, Q., Liu, Y., Tian, Y., Ding, T., Jiang, Z., Zhang, J., Gao, F., Dong, L., Bao, J., et al. (2020a). Dopamine sacrificial coating strategy driving formation of highly active surface-exposed Ru sites on Ru/TiO2 catalysts in Fischer-Tropsch synthesis. Appl. Catal. B Environ. *278*, 119261. https://doi.org/10.1016/j.apcatb.2020.119261.

Lyu, S., Wang, L., Li, Z., Yin, S., Chen, J., Zhang, Y., Li, J., and Wang, Y. (2020b). Stabilization of epsilon-iron carbide as high-temperature catalyst under realistic Fischer-Tropsch synthesis conditions. Nat. Commun. *11*, 6219.

Mogorosi, R.P., Fischer, N., Claeys, M., and Van Steen, E. (2012). Strong-metal-support interaction by molecular design: Fe-silicate interactions in Fischer-Tropsch catalysts. J. Catal. *289*, 140–150.

Mosayebi, A., and Haghtalab, A. (2015). The comprehensive kinetic modeling of the Fischer-Tropsch synthesis over Co@Ru/gamma-Al2O3 core-shell structure catalyst. Chem. Eng. J. *259*, 191–204.

Noreen, S., Bhatti, H.N., Iqbal, M., Hussain, F., and Sarim, F.M. (2020). Chitosan, starch, polyaniline and polypyrrole biocomposite with sugarcane bagasse for the efficient removal of Acid Black dye. Int. J. Biol. Macromol. *147*, 439–452.

Ojeda, M., Nabar, R., Nilekar, A.U., Ishikawa, A., Mavrikakis, M., and Iglesia, E. (2010). CO activation pathways and the mechanism of Fischer-Tropsch synthesis. J. Catal. *272*, 287–297.

Park, J.H., Wang, J.J., Xiao, R., Tafti, N., Delaune, R.D., and Seo, D.C. (2018). Degradation of Orange G by Fenton-like reaction with Fe-impregnated biochar catalyst. Bioresour. Technol. *249*, 368–376.

Phanopoulos, A., Pal, S., Kawakami, T., and Nozaki, K. (2020). Heavy-metal-free fischer-tropsch type reaction: sequential homologation of alkylborane using a combination of CO and hydrides as methylene source. J. Am. Chem. Soc. *142*, 14064–14068.

Raupp, G.B., and Delgass, W.N. (1979). Mossbauer investigation of supported fe and feni catalysts .2. Carbides formed by fischer-tropsch synthesis. J. Catal. *58*, 348–360.

Santos, V.P., Wezendonk, T.A., Delgado Jaen, J.J., Dugulan, A.I., Nasalevich, M.A., Islam, H.-U., Chojecki, A., Sartipi, S., Sun, X., Hakeem, A.A., et al. (2015). Metal organic framework-mediated synthesis of highly active and stable Fischer-Tropsch catalysts. Nat. Commun. *6*, 6451.

Sitthisa, S., An, W., and Resasco, D.E. (2011). Selective conversion of furfural to methylfuran over silica-supported Ni-Fe bimetallic catalysts. J. Catal. *284*, 90–101.

Srenscek-Nazzal, J., Kaminska, W., Michalkiewicz, B., and Koren, Z.C. (2013). Production, characterization and methane storage potential of KOH-activated carbon from sugarcane molasses. Ind. Crops Prod. *47*, 153–159.

Suo, H.Y., Wang, S.G., Zhang, C.H., Xu, J., Wu, B.S., Yang, Y., Xiang, H.W., and Li, Y.W. (2012). Chemical and structural effects of silica in iron-based Fischer-Tropsch synthesis catalysts. J. Catal. *286*, 111–123.

Tan, H.B., Tang, J., Henzie, J., Li, Y.Q., Xu, X.T., Chen, T., Wang, Z.L., Wang, J.Y., Ide, Y., Bando, Y., and Yamauchi, Y. (2018). Assembly of hollow carbon nanospheres on graphene nanosheets and creation of iron-nitrogen-doped porous carbon for oxygen reduction. Acs Nano *12*, 5674–5683.

Tan, P. (2016). Active phase, catalytic activity, and induction period of Fe/zeolite material in nonoxidative aromatization of methane. J. Catal. *338*, 21–29.

Tao, X., Xu, H., Luo, S., Wu, Y.Q., Tian, C.H., Lu, X.H., and Qing, Y. (2020). Construction of N-doped carbon nanotube encapsulated active nanoparticles in hierarchically porous carbonized wood frameworks to boost the oxygen evolution reaction. Appl. Catal. B *279*, 119367. https://doi.org/10.1016/j.apcatb.2020.119367.

Tao, H.-C., Zhang, H.-R., Li, J.-B., and Ding, W.-Y. (2015). Biomass based activated carbon obtained from sludge and sugarcane bagasse for removing lead ion from wastewater. Bioresour. Technol. *192*, 611–617.

Tauster, S.J., Fung, S.C., Baker, R.T.K., and Horsley, J.A. (1981). Strong-interactions in supported-metal catalysts. Science *211*, 1121–1125.

van Deelen, T.W., Mejia, C.H., and De Jong, K.P. (2019). Control of metal-support interactions in heterogeneous catalysts to enhance activity and selectivity. Nat. Catal. *2*, 955–970.

Wang, D., and Astruc, D. (2017). The recent development of efficient Earth-abundant transition-metal nanocatalysts. Chem. Soc. Rev. *46*, 816–854.

Wang, H., Huang, S., Wang, J., Zhao, Q., Wang, Y., Wang, Y., and Ma, X. (2019a). Effect of Ca promoter on the structure and catalytic behavior of FeK/Al2O3 catalyst in fischer-tropsch synthesis. Chemcatchem *11*, 3220–3226.

Wang, P., Chen, W., Chiang, F.K., Dugulan, A.I., Song, Y.J., Pestman, R., Zhang, K., Yao, J.S., Feng, B., Miao, P., et al. (2018). Synthesis of stable and low-CO2 selective epsilon-iron carbide Fischer-Tropsch catalysts. Sci. Adv. *4*, eaau2947.

Wang, S.X., Zou, K.X., Qian, Y.X., Deng, Y.F., Zhang, L., and Chen, G.H. (2019b). Insight to the synergistic effect of N-doping level and pore structure on improving the electrochemical performance of sulfur/N-doped porous carbon cathode for Li-S batteries. Carbon *144*, 745–755.

Wei, Y.X., Yan, L.L., Ma, C.P., Zhang, C.H., Sun, S., Wen, X.D., Yang, Y., and Li, Y.W. (2020). Mesoporous iron oxide nanoparticle-decorated graphene oxide catalysts for Fischer-Tropsch synthesis. Acs Appl. Nano Mater. *3*, 7182–7191.

Weststrate, C.J., Sharma, D., Rodriguez, D.G., Gleeson, M.A., Fredriksson, H.O.A., and Niemantsverdriet, J.W. (2020). Mechanistic insight into carbon-carbon bond formation on cobalt under simulated Fischer-Tropsch synthesis conditions. Nat. Commun. *11*, 750.

Wezendonk, T.A., Santos, V.P., Nasalevich, M.A., Warringa, Q.S.E., Dugulan, A.I., Chojecki, A., Koeken, A.C.J., Ruitenbeek, M., Meima, G., Islam, H.-U., et al. (2016). Elucidating the nature of Fe species during pyrolysis of the Fe-BTC MOF into highly active and stable fischer-tropsch catalysts. Acs Catal. *6*, 3236–3247.

Willinger, M.G., Zhang, W., Bondarchuk, O., Shaikhutdinov, S., Freund, H.-J., and Schloegl, R. (2014). A Case of strong metal-support interactions: combining advanced microscopy and model systems to elucidate the atomic structure of Interfaces. Angew. Chem. Int. Ed. *53*, 5998–6001.

Wu, J.H., Wang, L.C., Lv, B.L., and Chen, J.G. (2017). Facile fabrication of BCN nanosheet-encapsulated nano-iron as highly stable fischer-tropsch synthesis catalyst. Acs Appl. Mater. Interfaces *9*, 14319–14327.

Xu, K., Sun, B., Lin, J., Wen, W., Pei, Y., Yan, S., Qiao, M., Zhang, X., and Zong, B. (2014). epsilon-Iron carbide as a low-temperature Fischer-Tropsch synthesis catalyst. Nat. Commun. *5*, 5783.

Yan, Q., Wan, C., Liu, J., Gao, J., Yu, F., Zhang, J., and Cai, Z. (2013). Iron nanoparticles in situ encapsulated in biochar-based carbon as an effective catalyst for the conversion of biomass-derived syngas to liquid hydrocarbons. Green. Chem. *15*, 1631–1640.

Yang, C., Zhao, H., Hou, Y., and Ma, D. (2012). Fe5C2 nanoparticles: a facile Bromide-induced synthesis and as an active phase for fischer-tropsch synthesis. JACS *134*, 15814–15821.

Zhang, B., Song, J., Yang, G., and Han, B. (2014). Large-scale production of high-quality graphene using glucose and ferric chloride. Chem. Sci. *5*, 4656–4660.

Zhang, Q., Kang, J., and Wang, Y. (2010). Development of novel catalysts for fischer-tropsch synthesis: tuning the product selectivity. Chemcatchem *2*, 1030–1058.

Zhang, Y.R., Su, X., Li, L., Qi, H.F., Yang, C.Y., Liu, W., Pan, X.L., Liu, X.Y., Yang, X.F., Huang, Y.Q., and Zhang, T. (2020). Ru/TiO2 catalysts with size-dependent metal/support interaction for tunable reactivity in fischer-tropsch synthesis. Acs Catal. *10*, 12967–12975.

Zhang, Z.P., Sun, J.T., Wang, F., and Dai, L.M. (2018). Efficient oxygen reduction reaction (ORR) catalysts based on single iron atoms dispersed on a hierarchically structured porous carbon framework. Angew. Chem. Int. Ed. *57*, 9038–9043.

Zhao, X., Lv, S., Wang, L., Li, L., Wang, G., Zhang, Y., and Li, J. (2018). Comparison of preparation methods of iron-based catalysts for enhancing Fischer-Tropsch synthesis performance. Mol. Catal. *449*, 99–105.

Zhu, C.Z., Fu, S.F., Song, J.H., Shi, Q.R., Su, D., Engelhard, M.H., Li, X.L., Xiao, D.D., Li, D.S., Estevez, L., et al. (2017). Self-assembled Fe-N-doped carbon nanotube aerogels with single-atom catalyst feature as high-efficiency oxygen reduction electrocatalysts. Small *13*, 1603407. https://doi.org/10.1002/smll.201603407.

Zou, K.X., Deng, Y.F., Chen, J.P., Qian, Y.Q., Yang, Y.W., Li, Y.W., and Chen, G.H. (2018). Hierarchically porous nitrogen-doped carbon derived from the activation of agriculture waste by potassium hydroxide and urea for high-performance supercapacitors. J. Power Sources *378*, 579–588.

STAR★METHODS

KEY RESOURCES TABLE

REAGENT or RESOURCE	SOURCE	IDENTIFIER
Chemicals, peptides, and recombinant proteins		
$Fe(NO_3)_3 \cdot 9H_2O$	Sinopharm Chemical Reagent Co., Ltd.	CAS:7782-61-8
Activated carbon	Sinopharm Chemical Reagent Co., Ltd.	CAS:7440-44-0

RESOURCE AVAILABILITY

Lead contact

Further information and requests for resources and reagents should be directed to and will be fulfilled by the lead contact, Mingyue Ding (dingmy@whu.edu.cn).

Materials availability

This study did not generate new unique reagents.

Data and code availability

This study did not generate new datasets.

METHOD DETAILS

1. Catalyst preparation

The biosugarcane-based Fe/C_{bio} catalysts with different iron loading were prepared using impregnation method (Scheme 1). Typically, a certain amount of $Fe(NO_3)_3 \cdot 9H_2O$ was added into 200 mL of deionized water. Then ~1 mL HNO3 was slowly dropped to make sure the system was under a strong acid condition (pH<1). After stirring for 20 min, 2.0 g sugarcane bagasse (40–60 mesh) was dispersed into the above solution and stirred for 12 h at room temperature. The obtained solid was then dried at 100 °C overnight and subsequent pyrolysis at 450 °C (10 °C min^{-1}) for 2 h under N2 flow (200 ml min^{-1}). The acquired catalysts based on the weight loading of Fe were named as Fe_χ/C_{bio}, where χ = 1, 4, 8, or 12.

For comparison, the Fe_4/AC catalyst was also prepared by the same procedures, except for changing the biosugarcane support to activated carbon (AC).

2. Catalyst characterization

Scanning electron microscopy (SEM) and energy-dispersive X-ray spectroscopy (EDS) were carried out on TESCAN MIRA3 operated at 5.0 kV. Transmission electron microscope (TEM) and the high-resolution transmission electron microscopy (HRTEM) were performed on JEOL JEM 2100 operated at 200 kV. All Fe particles results from HRTEM analysis in our manuscript are calculated more than 100 nanoparticles at different regions by Nano Measurer 1.2 software. Nitrogen absorption/desorption measurements were conducted at -196 °C using a JWGB BK-100B to measure the specific surface area and pore size distribution of catalysts. The powder X-ray diffraction (XRD) was determined on a Bruker D8 advance operated at 40 kV and 40 mV, with Cu-Kα radiation (λ = 1.5406 Å, 2θ =10–80°). X-ray photoelectron spectroscopy (XPS) was carried out on a Thermo ESCALAB 250XI with Al Kα (hν = 1486.6 eV), and the C 1s peak at 284.8 eV was used as a reference. The Raman spectra of as-prepared catalysts was recorded using a Horiba Evolution with a 532 nm laser beam. Fourier transform infrared spectra (FTIR) were detected using a NICOLET 5700 FTIR Spectrometer. The reducibility of catalysts was investigated by hydrogen temperature-programmed reduction (H_2-TPR) on a chemisorption analyzer (HUASI DAS-7000). Approximately 50 mg of catalyst loaded in a quartz tube was dehydrated first in N_2 (30 mL min^{-1}) from 20 to 350 °C (5 °C min^{-1}) and keeping 1 h. After cooling down to the room temperature, the catalyst was reduced in H_2 (5% H_2/N_2, 30 mL min^{-1}) from 50 to 800 °C (8 °C min^{-1}). H_2 temperature-programmed desorption (H_2-TPD) with mass spectrometry was carried out using a Bel Ctat II. About 50 mg of catalyst was used and reduced in H_2 (50 mL min^{-1}) from 20 to 350 °C (10 °C min^{-1}) and keeping 1 h. The catalyst was flushed at the same temperature with Ar gas

(50 mL/min) for 30 min. After cooling down to 50 °C, H_2 flow (50 mL/min) was continued for 30 min for adsorption. The system was then purged with Ar gas (50 mL/min) for 30 min to remove physisorbed H_2. The H_2-TPD was conducted from 50 to 800 °C at a rate of 10 °C min^{-1}. Mass change in a sample as a function of temperature was determined by thermogravimetric analysis (TGA) using a TGA55 operated from room temperature to 1000 °C with a ramping rate of 10 °C min^{-1} under N_2 flow. Induced coupled plasma-optical emission spectrometry (ICP-OES) on an Agilent 720ES was used to determine the iron loading of as-prepared catalysts. The carbon, nitrogen and hydrogen content were conducted by an elemental analyzer (RARIO EL III).

3. Catalyst evaluation

The catalytic performance of catalysts was conducted in a fixed bed reactor. About 100 mg of catalyst, sieved into 40–60 meshes, was mixed with the same volume of quartz granules (40–60 mesh) and packed into a stainless reaction tube. The catalyst was reduced in pure H2 at 350 °C, 0.1 MPa, 50 mL min^{-1} for 600 min. After that, the FTS reaction was carried out in syngas (H2/CO/N2 = 47.5/47.5/5.0, molar ratio) at 300 °C, and 2MPa. The samples were conducted at least for 30 h to reach a stable catalytic performance and then the catalytic performance results were obtained from the average of ten chromatographic automatic injections every one hour with carbon balance in the range 100 $\pm$ 5%. Gas products were online analyzed using a gas chromatograph (FULI GC 97) equipped with a thermal conductivity detector (TCD) and a flame ionization detector (FID). Porapak Q packed column (I.D = 3 mm) and 5A MolSieve packed column (I.D = 3 mm) were connected to TCD and RB-PLOT Al2O3 capillary column (I.D = 0.32 mm) was connected to FID. Liquid products were collected by cold traps and analyzed off-line using another gas chromatograph (FULI GC 97) equipped with a flame ionization detector (FID) and a RB-5 capillary column (I.D = 0.32 mm).